Article

Statistical Approach to Spectrogram Analysis for Radio-Frequency Interference Detection and Mitigation in an L-band Microwave Radiometer

Myeonggeun Oh and Yong-Hoon Kim *

School of Mechatronics, Gwangju Institute of Science and Technology, 123 Cheomdangwagi-ro, Buk-gu, Gwangju, 61005, Republic of Korea; mgoh1815@gmail.com (M.O.)

* Correspondence: yhkim@gist.ac.kr (Y.-H.K.); Tel.: +82-062-715-2387

Abstract: For the elimination of radio-frequency interference (RFI) in a passive microwave radiometer, the threshold level is generally calculated from the mean value and standard deviation. However, a serious problem that can arise is an error in the retrieved brightness temperature from a higher threshold level owing to the presence of RFI. In this paper, we propose a method to detect and mitigate RFI contamination using the threshold level from statistical criteria based on a spectrogram technique. Mean and skewness spectrograms are created from a brightness temperature spectrogram by shifting the 2-D window to discriminate the form of the symmetric distribution as a natural thermal emission signal. From the remaining bins of the mean spectrogram eliminated by RFI-flagged bins in the skewness spectrogram for data captured at 0.1-s intervals, two distribution sides are identically created from the left side of the distribution by changing the standard position of the distribution. Simultaneously, kurtosis calculations from these bins for each symmetric distribution are repeatedly performed to determine the retrieved brightness temperature corresponding to the closest kurtosis value of three. The performance is evaluated using experimental data, and the error in the retrieved brightness temperature is observed to be less than approximately 3 K from a window with a size of 100 × 100 time-frequency bins according to the RFI levels and cases.

Keywords: microwave radiometer; kurtosis; skewness; spectrogram; radio-frequency interference (RFI)

1. Introduction

The presence of radio-frequency interference (RFI) is a significant issue in radiometric measurements, caused potentially by any types of electromagnetic emissions, such as those by communication and navigation systems. Even if microwave radiometry is utilized for measuring sea salinity and soil moisture within the protected bandwidth range of 1400 to 1427 MHz, RFI can still degrade radiometric measurements owing to leakages from adjacent bands [1,2]. Several methods have been developed to detect and mitigate the presence of RFI. A powerful means of RFI detection and mitigation is the use of the kurtosis technique, which can be computed using the fourth central moment divided by the square of the second central moment [2–6]. The kurtosis value is equal to three if the received signal is RFI-free data; however, kurtosis uncertainty arises owing to a finite number of samples. Moreover, the kurtosis value can still be three for signal types such as the chirp and sinusoidal RFI signals. In other methodologies, RFI can be eliminated using time and frequency-domain techniques [7–9]. However, a method based on only one technique can not sufficiently remove contaminated RFI signals [10–12]. Recently, a multi-domain technique that combines a brightness temperature spectrogram, kurtosis spectra, and a time-domain plot was introduced for the Soil Moisture Active Passive (SMAP) mission [10]. From experimental results, the presence of various types of RFI signals was more clearly detected using the spectrogram technique than by using

any other techniques. Specifically, chirp RFI signals were not observed in the time domain and kurtosis spectra. To eliminate RFI contamination in the brightness temperature spectrogram, the threshold level of the brightness temperature spectrogram was calculated as $m+\beta\sigma$ for the lowest 90% of the corresponding bins, where m is the mean value, β is the threshold multiplier, and σ is the standard deviation. However, a higher threshold level can be determined if the presence of RFI exceeds the highest 10% in those bins. Thus, the selection of a constant percentage for those bins leads to an error in the retrieved brightness temperature. Although the RFI is eliminated via the increased threshold level, significant error will arise. As an alternative to the spectrogram technique, an image processing technique was employed using a smoothing algorithm [13]. In these results, various RFI signal types must be considered to determine the threshold multiplier for outdoor experiments beforehand, as threshold multipliers for the optimum threshold depend on RFI signal types with different values.

The aim of this paper is to demonstrate RFI detection capabilities and to present a mitigation algorithm for the purpose of minimizing potential errors originating from the sample intensity level using the threshold level from statistical criteria based on a spectrogram technique. A discussion of the proposed method follows in Section 2. This experiment was performed using a microwave radiometer system operating on the L-band. The instrument and test setup are described in Section 3. The experimental results and analysis are presented in Section 4, and the conclusion is presented in Section 5.

2. Proposed RFI Detection and Mitigation Algorithm

Recent research shows that the spectrogram technique is superior when used to observe various types of RFI signals compared with other techniques [10]. Based on the spectrogram technique, the procedures for RFI detection and mitigation are shown in Figure 1. The power spectrogram can be obtained from a data stream at the digital backend. The size of power spectrogram depends on several parameters such as the total number of signal samples, the window used for the FFT calculation of the data segments, and overlapping between these data segments. The power spectrogram was computed from each 0.1-sec data of 3.2 Msamples, and Hanning window size of 40,000 samples with overlapping of 6.25%. Thus, a power spectrogram with a size of 1265×1025 for the time and frequency bins is created with a resolution of 0.1s/1265≈79 μs and 15 MHz/1025≈14.6 kHz. Subsequently, the radiometric calibration is performed for the brightness temperature spectrogram as shown in Figure 2a. Each brightness temperature spectrogram is smoothed using a median filter with a size of 8×8 as shown in Figure 2b. The presence of RFI can be detected using the threshold level from the intensity of the bins in the brightness temperature spectrogram; however, this method incurs a considerable amount of error according to the RFI level and the number of selected bins in the brightness temperature spectrogram. To determine the retrieved brightness temperature, the subsequent steps are described as follows.

2.1. Step 1: Statistical Thresholding using Skewness

For RFI-free data, the distribution of all bins in power spectrogram might not have the form of a Gaussian distribution because the magnitude of the frequency response corresponding 15 MHz bandwidth is not uniform (flat) due to the flatness of analog band-pass filter and the low-pass filter in L-band radiometer given in Section 3. That would require a uniform magnitude of response up to the bandwidth, ununiformed magnitude of frequency response can be solved from the radiometric calibration by the spectrograms of an active cold source and matched load as different known temperature sources. The distribution of all bins in the brightness temperature spectrogram has the form of a Gaussian distribution. The received signals that are combined of the natural thermal emission signal and the RFI contamination show that the mass of the distribution is concentrated on the right tail because the RFI level is higher than the natural thermal emission signal. Thus, the presence of RFI can initially be detected from the asymmetry of the distribution by means of a skewness calculation. The skewness can be defined as

$$\gamma_1 = \frac{\mu_3}{\sigma^3}, \qquad (1)$$

where σ and μ_3 are the standard deviation and the third central moment, respectively. The calculated skewness value is equal to zero if the received signal has a symmetric distribution. From the shift of the 2-D window with a size of N × N time-frequency bins in the brightness temperature spectrogram at a constant size, the skewness levels from the bins in each window are computed to determine the asymmetry of the distribution, as shown in Figure 3. In this work, 2-D rectangular windows are used to reduce the error in the skewness on the side of the brightness temperature spectrogram. A small window can increase the uncertainty of the skewness, whereas a large window causes many bins in the skewness spectrogram to disappear considering the RFI contamination. The threshold level in the skewness spectrogram was computed as zero plus three times the standard deviation, i.e., $3\sigma_1$, where σ_1 is the standard deviation of all bins in the skewness spectrogram. Using a value of zero can serve as an accurate reference rather than the mean value from the constant percentage of bins in the brightness temperature spectrogram [10]. Subsequently, RFI-flagged bins in the skewness spectrogram in Figure 2d are reflected in the mean spectrogram as shown in Figure 2f.
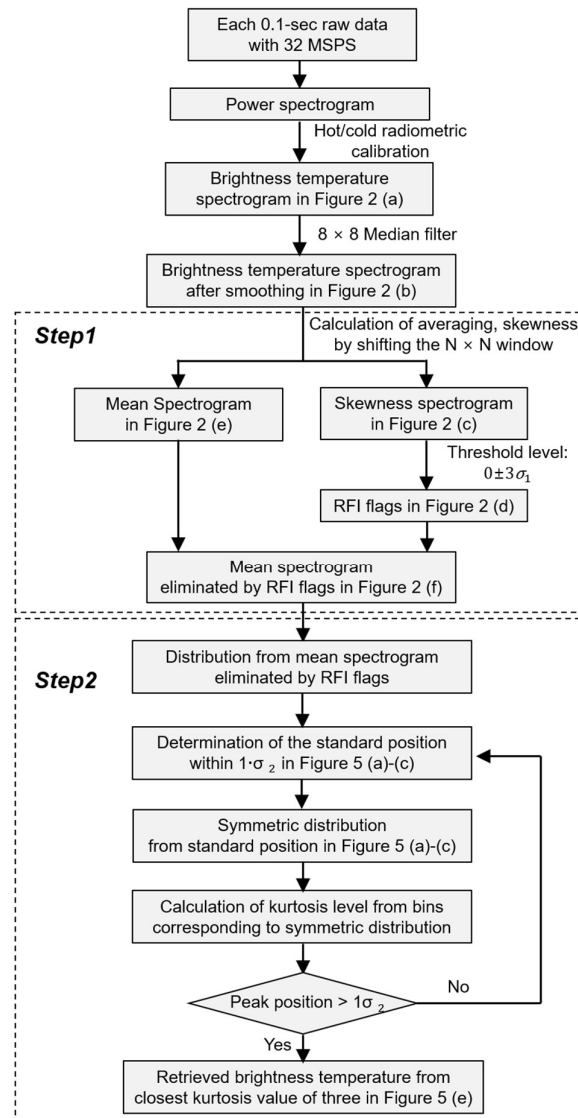

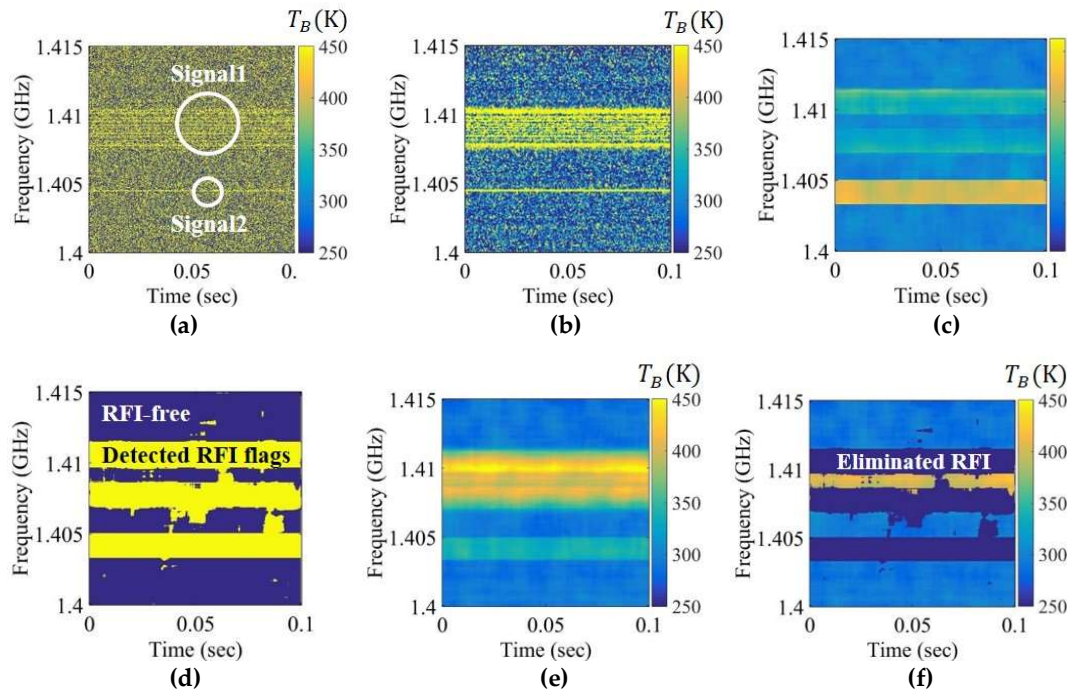**Figure 1.** Flowchart of the proposed process.

Figure 2. Example spectrograms of RFI-contaminated signals corresponding to each procedure in Step 1: (a) Brightness temperature spectrogram; (b) Brightness temperature spectrogram after smoothing; (c) Skewness spectrogram; (d) RFI flags in a skewness spectrogram after thresholding; (e) Mean spectrogram; (f) Mean spectrogram eliminated by RFI-flagged bins.
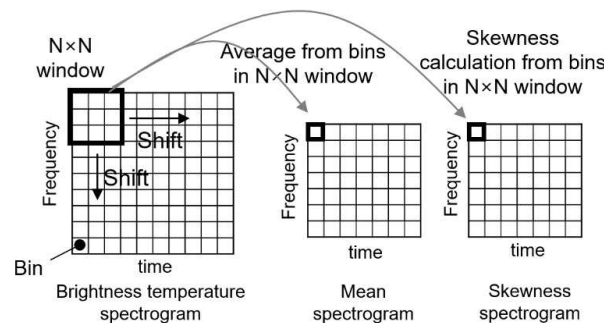

Figure 3. Process of obtaining the mean and skewness spectrograms.

In this step, the skewness spectrogram is used to remove the RFI that can be detected. Similarly, RFI removal using kurtosis is also possible. Figure 4 shows the results of the skewness spectrogram and kurtosis spectrogram for a performance comparison. The kurtosis spectrogram can be obtained through the same procedure used to create the skewness spectrogram as shown in Figure 3. RFI contamination can be observed in the two spectrograms in Figures 4a,b; however, the removal results in Figures 4c,d are different when the threshold levels of the kurtosis spectrogram and skewness spectrogram are applied as $3+3\sigma$ and $0+3\sigma$ in those bins, respectively. Consequently, the skewness spectrogram shows that the performance of RFI elimination is better owing to the effect on the standard deviation and uncertainty of each spectrogram. Step 1 eliminates the detected RFI signals with not only a high level of the RFI signal but also a low level of the thermal signal, having the characteristics of an asymmetric distribution in the window. Specifically, the elimination of low-level signals is an important procedure to create a symmetric distribution from bins in the mean spectrogram reflected by RFI-flagged bins because the bins on the left side of the distribution affect the computed kurtosis value in Step 2.
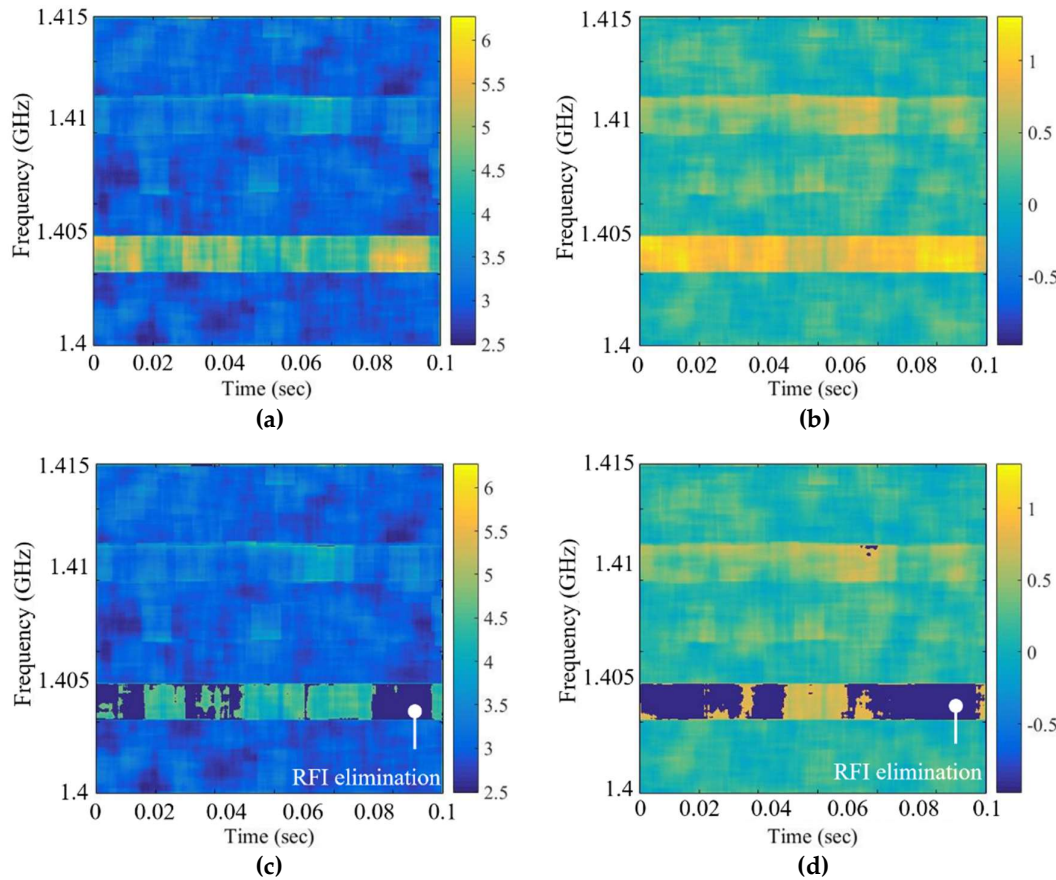
Figure 4. Example spectrograms applied to RFI-contaminated signals of 25 K. (a) Kurtosis spectrogram; (b) Skewness spectrogram; (c) Kurtosis spectrogram after thresholding; (d) Skewness spectrogram after thresholding.

2.2. Step 2: Process of Obtaining the Retrieved Brightness Temperature using Kurtosis

From the remaining bins of the mean spectrogram reflected by RFI-flagged bins in the skewness spectrogram in Figure 2f, the distribution can be represented as the solid lines (black lines) in Figure 5a. However, it might have the form of a non-Gaussian distribution owing to the unremoved RFI bins of the skewness spectrogram. The bins at the brightness temperature of approximately 400 K in Figure 5a are unremoved RFI contaminations at 1.409 GHz in Figure 2f. As the bins corresponding to the left tail of the distribution (solid line in Figure 5a) are relatively less affected by the RFI, two identical sides of distribution, i.e., symmetric distribution, can be created from the left tail of the distribution on the basis of specific points on the distribution, i.e., standard positions. The examples of three cases of symmetric distributions corresponding to the standard positions of 295, 300, and 305 K are shown as dotted lines in Figures 5a-c. In other words, the symmetric distributions have the same values of mean, median, and mode. Figure 5d shows the all bins corresponding each symmetric distribution in Figures 5a-c, and subsequently, three cases of kurtosis values in Figure 5e can be obtained as 2.12, 2.75, and 3.26 for standard position of 295, 300, and 305 K, respectively. In the same manner, kurtosis curve as a solid line (black line) in Figure 5e can be obtained from the repeated kurtosis computation from the corresponding bins of each symmetric distribution by changing the standard position on the distribution (solid line in Figure 5a) with an interval of 0.1 K within $1 \cdot \sigma_2$, where σ_2 is the standard deviation of the mean from the remaining bins in Figure 2f, i.e., 68 % of data values. Here, the standard position in Figure 5e can be considered as the brightness temperature, and the retrieved brightness temperature over 0.1-s data can be obtained from the closest kurtosis value of three in Figure 5e.
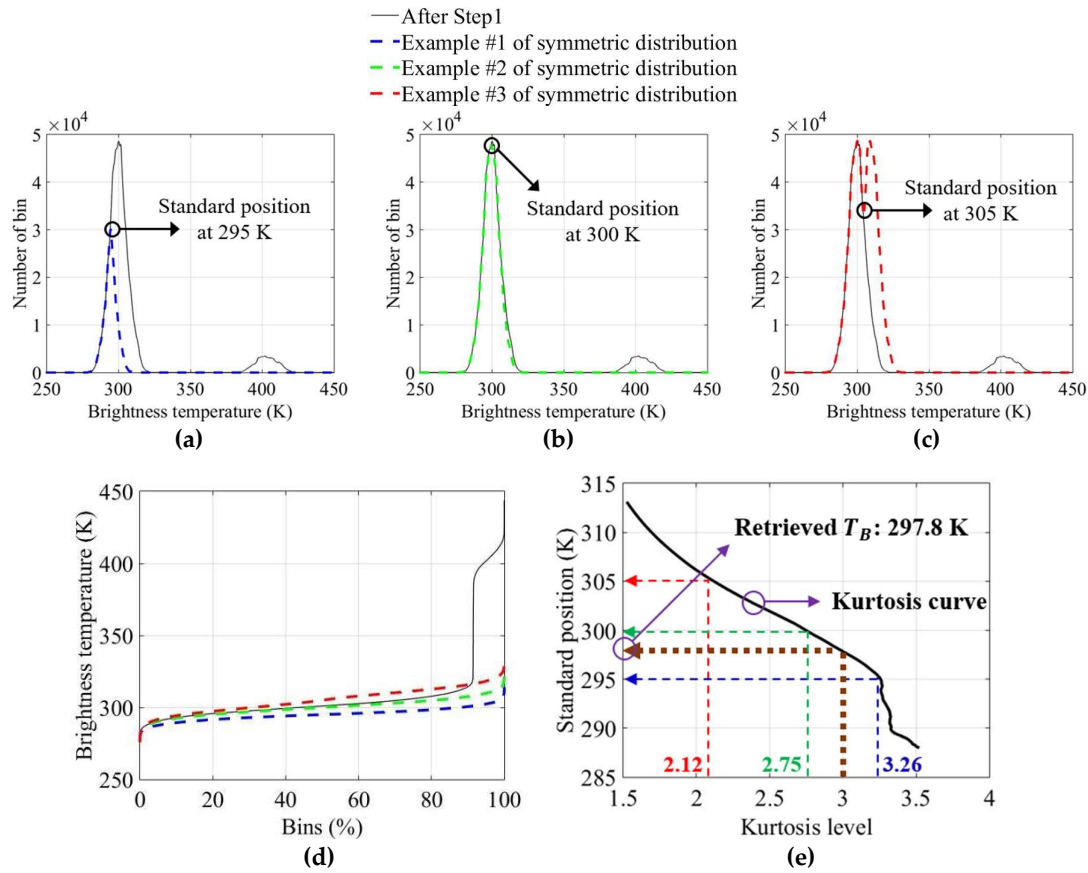
Figure 5. (a)-(c) Solid line (black line) represents the distribution from the remaining bins in Figure 2f, and dotted lines (colored lines) are the examples of symmetric distributions from the standard positions of 295, 300, and 305 K, respectively; (d) Brightness temperature versus the intensity percentage of symmetric distribution corresponding to (a)-(c); (e) Standard position of symmetric distribution versus kurtosis level.

3. L-band Microwave and Experimental Setup
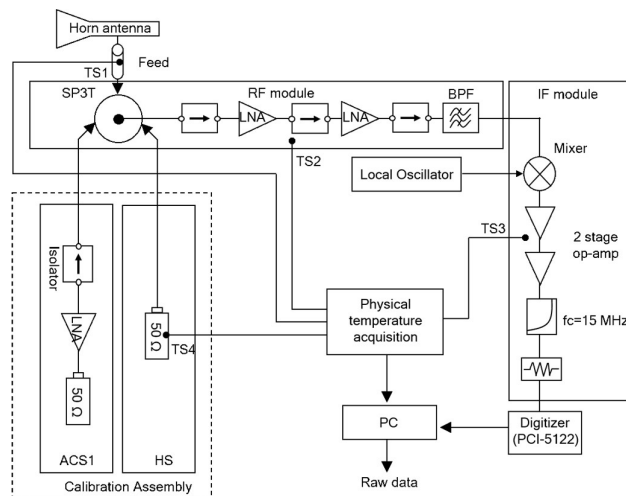
3.1. L-band Radiometer Description

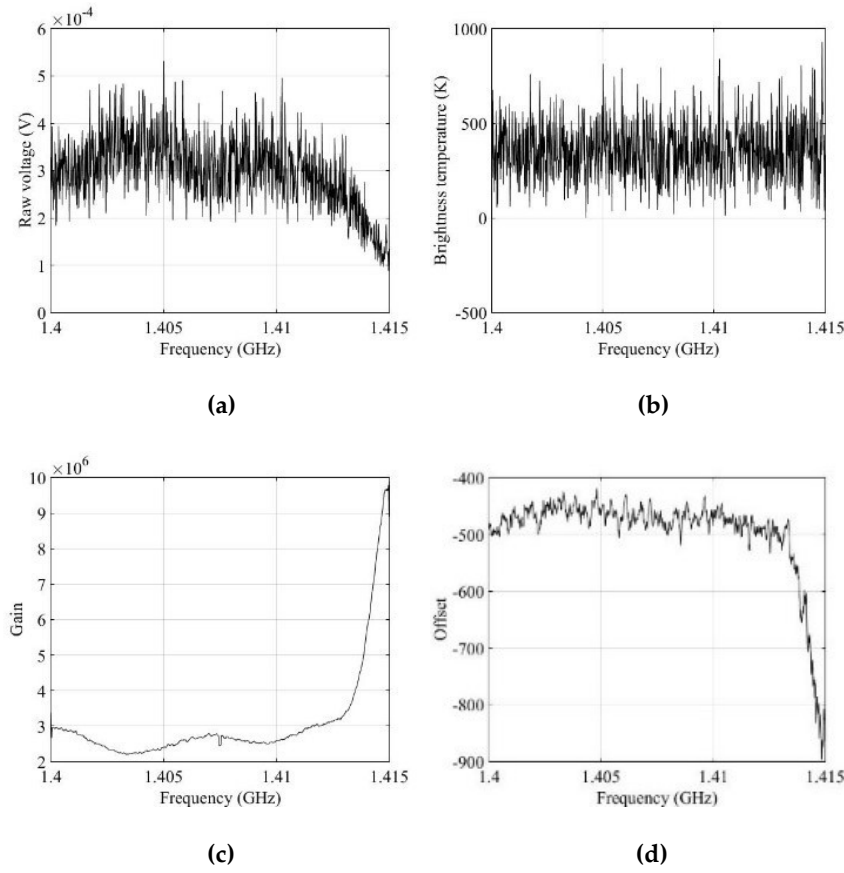**Figure 6.** Block diagram of the developed L-band radiometer.

Figure 7. Radiometer calibration: (a) Raw voltage data over a 0.1-s data; (b) Brightness temperatures after radiometer calibration; (c) Gain values; (d) Offset values.

Figure 6 shows a block diagram of the developed L-band radiometer as a heterodyne receiver. The radiometer receiver can be operated either as a total power radiometer in the measurement mode or in the calibration mode [14]. In the calibration mode, two-point calibration was performed using active cold sources (ACS) and a matched load (ML) as different known noise temperatures [15,16]. The analog front-end downconverts the bandwidth of 15 MHz from 1.4 to 1.415 GHz, and the samples are obtained from the digital backend at 32 MSPS with 14 bits. From data at 0.1-s intervals, each power spectrogram is calibrated to make uniformity of each frequency channel in the passband of the radiometer using two known calibration sources for the corresponding 0.1-s file as shown in Figure 7 [10]. Smoothing is performed using a median filter with a size of 8 × 8 in the calibrated spectrogram. The value of each bin in the brightness temperature spectrogram, T_B, can be calculated as in an earlier work [10],

$$G = (T_{ML} - T_{ACS})/(V_{ML} - V_{ACS}),$$
$$O = T_{ML} - V_{ML} \cdot G,$$
$$T_{b,i} = G \times V_i + O, \tag{2}$$

where T_{ML} and T_{ACS} are, respectively, the known hot and cold temperatures of the reference sources, V_{ML} and V_{ACS} are the corresponding mean voltages of the power spectrogram for the corresponding frequency bins, V_i is the voltage of each bin in the power spectrogram, and G and O are the gain and offset values from the radiometer calibration, respectively. The recorded data from the digital backend in each 1.5-s data file are divided into the measurement mode from the antenna (~1 s) and the calibration mode (~0.5 s). The temperature sensors were attached to critical radiometer components for temperature drift compensation. These were a standard gain horn

antenna feed, an RF module, and an IF module for the calibration source [17]. The detailed instrument specifications of the radiometer are listed in Table 1.

Table 1. Instrument specifications of the developed L-band radiometer

Index	Parameter
Frequency range	1.4−1.415 GHz
Antenna Gain (dB)	10 Typ.
Radiometry sensitivity	< 0.13 K
Radiometry stability	< 0.2 K over a period of 1 h
Radiometry accuracy	< 1 K over a period of 1 h
Integration time	1 s

3.2. Experimental Setup
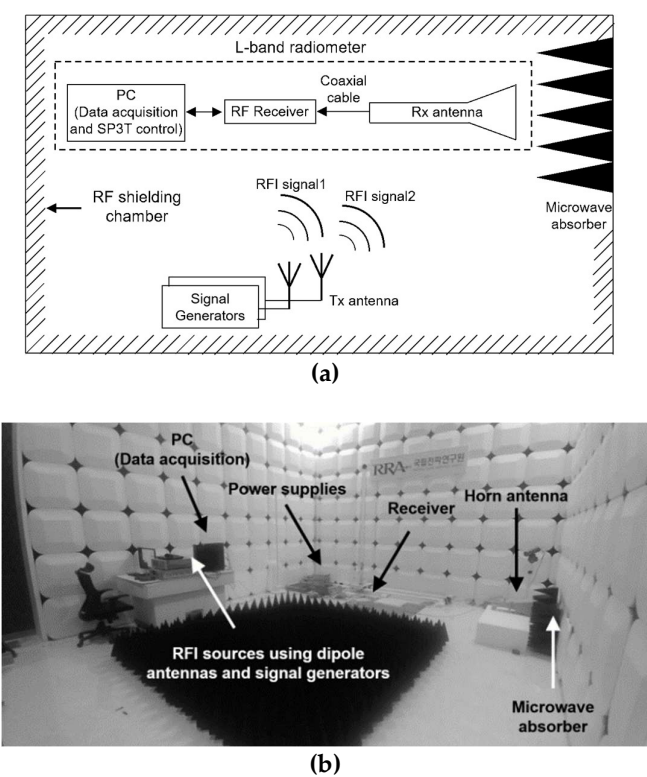

(a)

(b)

Figure 8. (a) Experimental setup; (b) Photograph of the RFI test.

Figure 8 shows the experimental setup in the RF shielding chamber used. A pyramid-type microwave absorber was positioned in front of the horn antenna of the microwave radiometer for measuring the absorber temperature of 296 K. For the true value of the brightness temperature, the generated thermal noise signal, i.e., RFI-free data, is received when the signal generators are turned off. For the performance verification of the proposed algorithm, arbitrary RFI signals are generated using two signal generators and dipole antennas. The thermal noise signal of the microwave absorber and the generated RFI signals are simultaneously obtained when the signal generators are turned on. Thus, the errors of the retrieved brightness temperature can be obtained from the difference between cases where signal generators are turned on and off. These are applied to the proposed RFI detection and mitigation algorithm, and the experiments are performed according to the RFI types and levels from the signal generators.

4. Experimental Results and Analysis

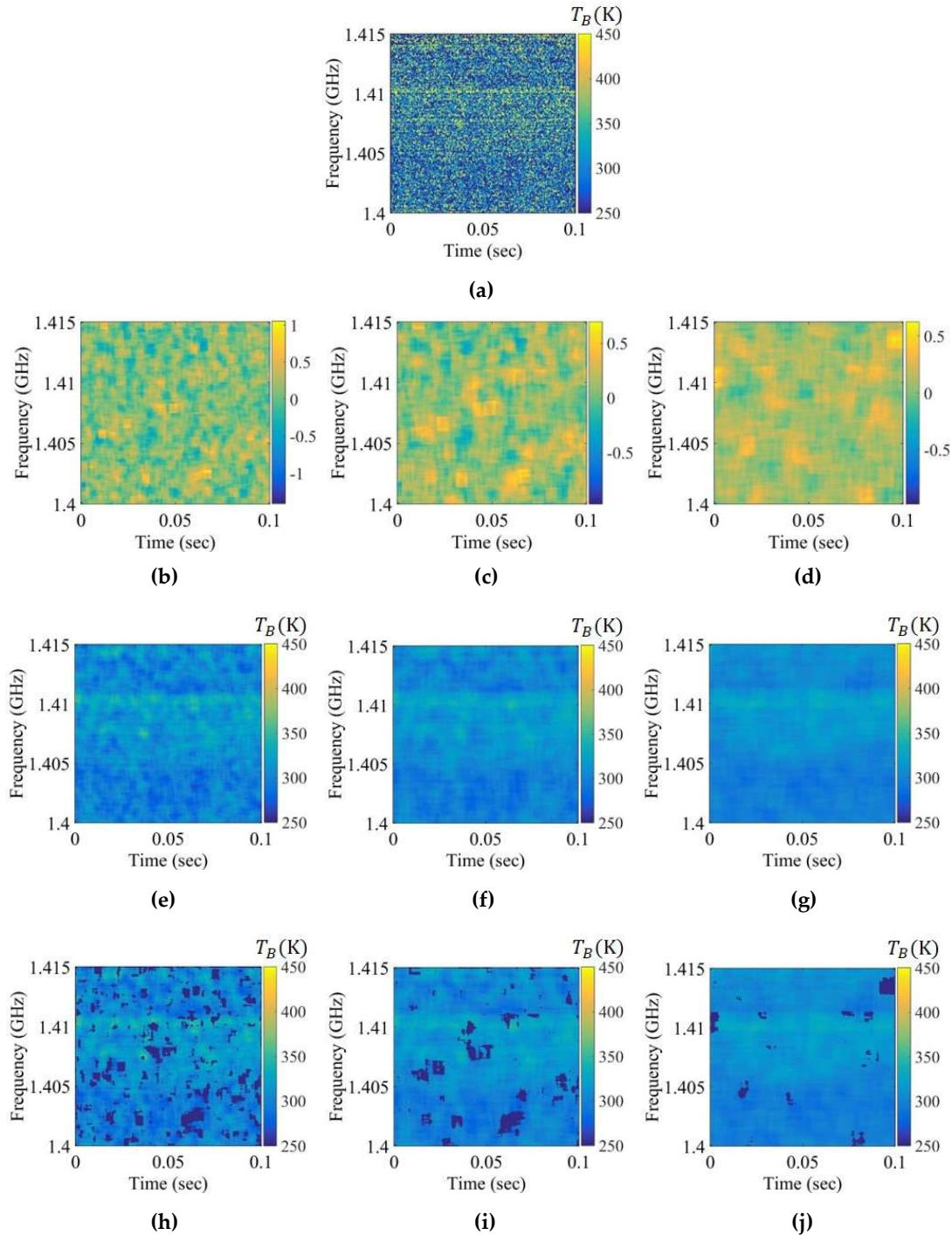### 4.1. Experimental Results of Steps

Figure 9. Spectrograms applied to the chirp RFI signal to a level below approximately 10 K over the entire 1.407 to 1.411 GHz band. (a) Brightness temperature spectrogram after smoothing; (b)-(d) Skewness spectrograms obtained using the window sizes of 50 × 50, 75 × 75, and 100 × 100, respectively; (e)-(g) Mean spectrograms obtained using the window sizes of 50 × 50, 75 × 75, and 100 × 100, respectively; (h)-(j) Mean spectrograms after Step 1 obtained using the window sizes of 50 × 50, 75 × 75, and 100 × 100, respectively.
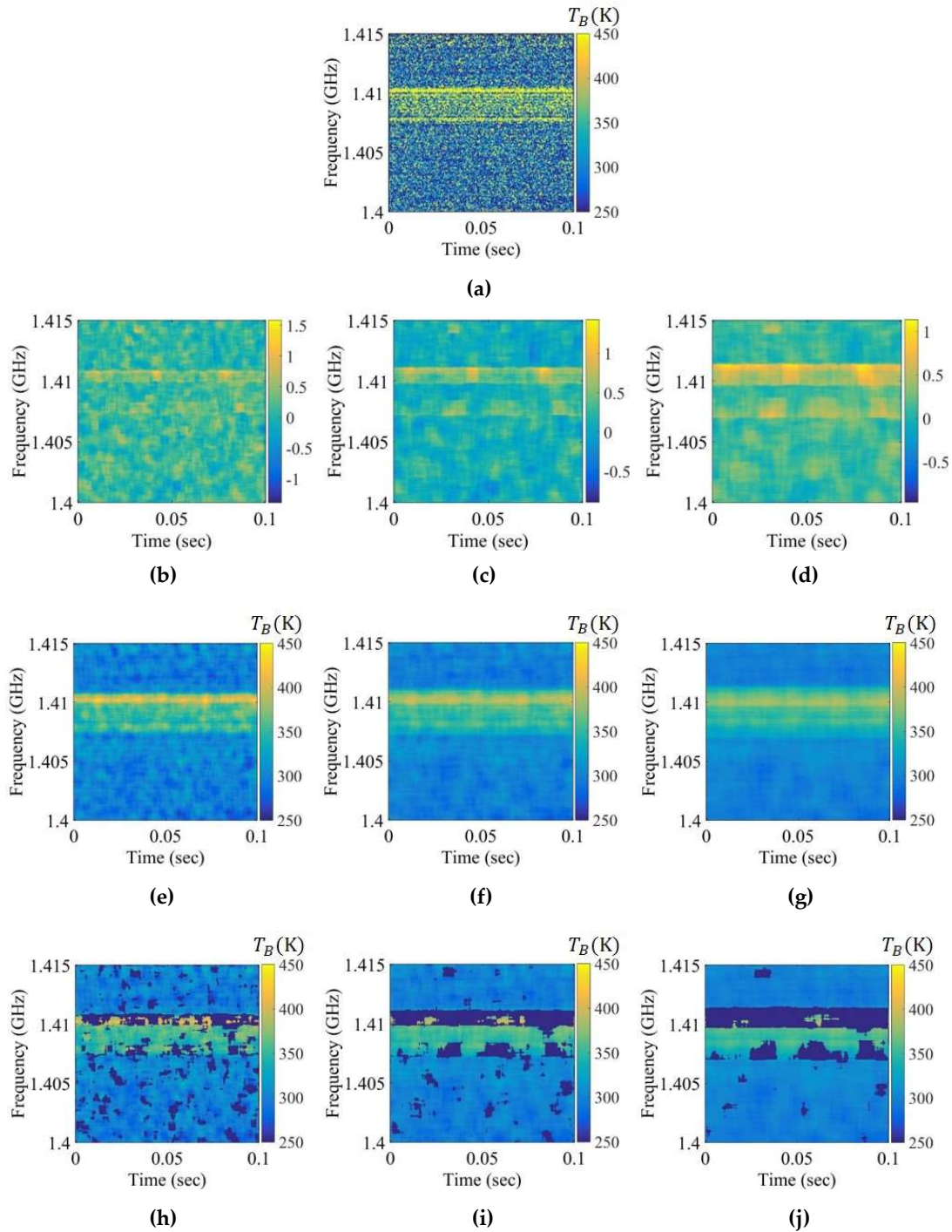
Figure 10. Spectrograms applied to the chirp RFI signal to a level below approximately 50 K over the entire 1.407 to 1.411 GHz band. (a) Brightness temperature spectrogram after smoothing; (b)-(d) Skewness spectrograms obtained using the window sizes of 50 × 50, 75 × 75, and 100 × 100, respectively; (e)-(g) Mean spectrograms obtained using the window sizes of 50 × 50, 75 × 75, and 100 × 100, respectively; (h)-(j) Mean spectrograms after Step 1 obtained using the window sizes of 50 × 50, 75 × 75, and 100 × 100, respectively.
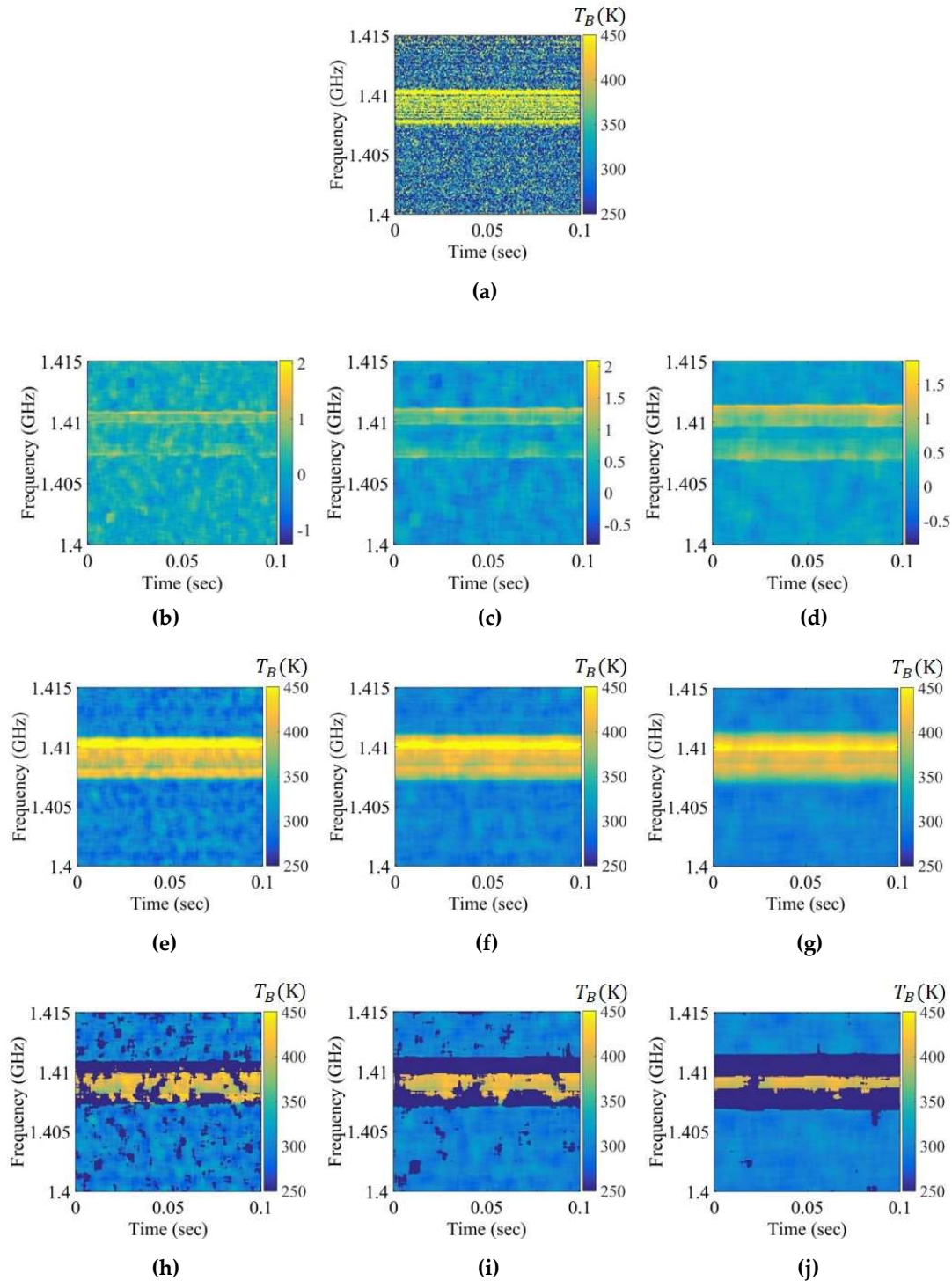
Figure 11. Spectrograms applied to the chirp RFI signal to a level below approximately 100 K over the entire 1.407 to 1.411 GHz band. (a) Brightness temperature spectrogram after smoothing; (b)-(d) Skewness spectrograms obtained using the window sizes of 50 × 50, 75 × 75, and 100 × 100, respectively; (e)-(g) Mean spectrograms obtained using the window sizes of 50 × 50, 75 × 75, and 100 × 100, respectively; (h)-(j) Mean spectrograms after Step 1 obtained using the window sizes of 50 × 50, 75 × 75, and 100 × 100, respectively.
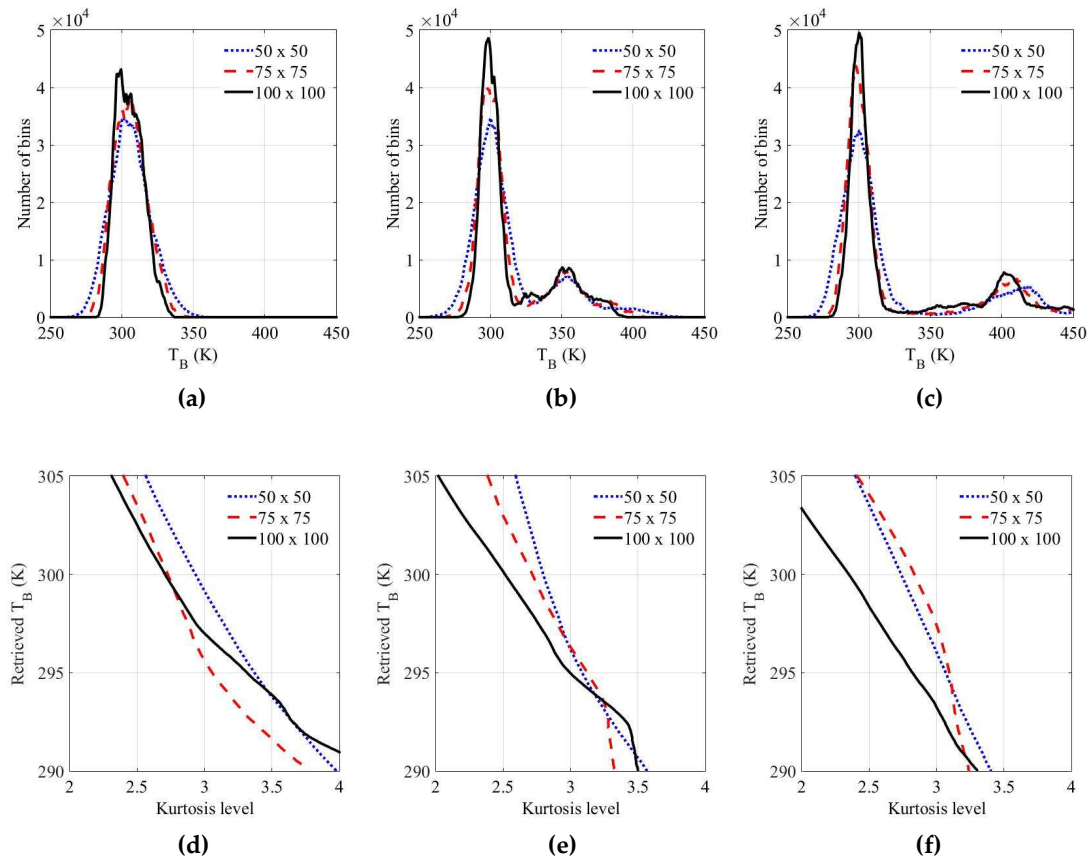
Figure 12. Processing results in Step 2. (a)-(c) Distribution from the bins of the mean spectrogram eliminated by RFI-flagged bins in the skewness spectrogram when the RFI levels are 10, 50, and 100 K, respectively; (d)-(f) Retrieved brightness temperature versus the kurtosis level when the RFI levels are 10, 50, and 100K, respectively.

For a comparison, Figures 9-11 depict the experimental results for RFI chirp signals of approximately 10, 50, and 100 K level in Step 1. In the case of a weak RFI signal of the level approximately 10 K in Figure 9, it is difficult to discriminate between the natural thermal emission signal and the RFI signal in the brightness temperature spectrogram and the skewness spectrogram because the skewness value calculated from the bins of the RFI signals and the thermal emission signals is less than the uncertainty of the skewness value calculated from the thermal emission signal. However, this signal appears in the mean spectrogram with a blurring effect. The RFI flags of the mean spectrogram become larger than those of the brightness temperature when the window size is increased. The relatively strong RFI signals of levels approximately 50 and 100 K are detected in the spectrograms in Figures 10 and 11; however, the skewness spectrogram does not eliminate the high level of RFI in the form of a Gaussian distribution. The boundaries of the RFI signal and the natural thermal emission signal in the brightness temperature spectrogram can be reliably eliminated; however, the distribution will remain symmetric if the window is covered by a wide-band RFI signal. This is not an issue here because the high level of the RFI signal is separated from the natural thermal emission signal via the distribution in the example of 350 and 400 K in Figures 12b,c, respectively. Thus, a high level of RFI signal, e.g., RFI levels of 350 and 400 K, can be ignored from the symmetric distributions realized by shifting the standard position of the distribution in Step 2. Figures 12d-f display the retrieved brightness temperature corresponding to each kurtosis level. According to the results, the kurtosis levels gradually decrease when the standard position of the distribution is increased. The retrieved brightness temperature can be selected from the closest value of three.

4.2. Error Analysis and Comparison between the Privious Method and Proposed Method
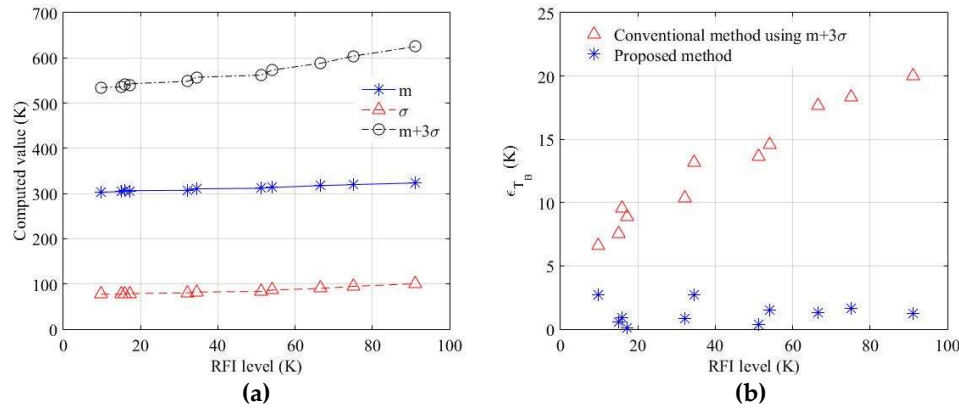

Figure 13. (a) Computed values from the bins in the brightness temperature spectrogram versus the level of chirp RFI signal occupied by the entire 1.407 to 1.411 GHz band; (b) Error comparison of the conventional and proposed methods.

Table 2. Maximum error of the retrieved brightness temperature (K) for different cases of RFI signals with the RFI level up to ~ 100 K

RFI signal case	Max. ε_{T_B} (K) for window size		
	50×50	75×75	100×100
Chirp signal	4.53	3.10	2.71
AM signal	3.69	3.07	2.89
Continuous signal	3.58	3.66	2.54
Pulsed signal	3.78	3.15	2.87
Continuous signal, pulsed signal	2.31	3.23	2.57
AM signal, pulsed signal	2.81	2.41	2.24
AM signal, continuous signal	3.95	2.43	2.76
Chirp signal, continuous signal	4.57	3.43	2.78
Chirp signal, pulsed signal	4.67	3.66	2.81
Chirp signal, AM signal, continuous signal	4.28	3.28	2.82

Figures 9-12 show the experimental results obtained using the chirp RFI signal. Similarly, ten RFI signals and three window sizes were tested. The chirp RFI signal occupies the entire 1.407 to 1.411 GHz band, and the AM signal is a sinusoidal signal at 1.4045 GHz, modulated by a pulse train with a pulse width of 2 μs and pulse repetition frequency of 360 Hz with a 1 % duty cycle of the pulse train. The pulsed RFI signal has a pulse period of 24 μs and a pulse width of 8 μs. The maximum errors of the retrieved brightness temperature are summarized in Table 2. The results in Table 2 are presented for RFI cases and levels with the same property such as duty cycle and period. The best performance is obtained with a window size of 100 × 100, and the error of the retrieved brightness temperature, ε_{T_B}, as tested is less than approximately 3 K. A larger window size shows that the error of the retrieved brightness temperature can be reduced. In the proposed method, the error of the retrieved brightness temperature can be relatively minimized for the wideband RFI signal. The threshold levels of the previous method are calculated as the mean value plus a few times the standard deviation from the selection of a constant percentage for the data sample [2,9,10]. However, a higher threshold level can be determined if the presence of RFI covers the wideband and long time period. Figure 13a shows the change in the conventional threshold level using *m+βσ* according to the RFI level. Owing to the higher mean value and the standard deviation with the increase in the RFI level in the experimental environment of 296 K, the RFI can be properly unremoved owing to the higher bias. Figure 13b shows that, in the conventional method, the error of the brightness temperature increases from the increased RFI level. Moreover, the selection of a constant percentage

for these samples leads to erroneous results for the retrieved brightness temperature. This error will be proportionally increased when the RFI is spread over a wider range. However, the proposed method can solve the problem of bias from zero in the skewness spectrogram instead of the mean value, and an appropriate value of the retrieved brightness temperature can be determined using kurtosis. It is shown that the presence of RFI can reduce errors in a wideband and over a long period as much as possible. However, if the RFI contamination covers the entire spectrogram, it is very difficult to determine the retrieved brightness temperature because the RFI contamination in the mean spectrogram and skewness spectrogram will be entirely covered.

5. Conclusion

This paper describes a novel RFI detection and mitigation algorithm based on the spectrogram technique using the threshold level from statistical criteria. The proposed procedure is demonstrated with statistical approaches using skewness and kurtosis. In the experimental results, the error of the retrieved brightness is shown to be less than approximately 3 K with a window size of 100×100 from ten cases of RFI signals according to changes in the RFI level up to 100 K. The uncertainty of each bin in the skewness spectrogram can be reduced using a larger window size, and threshold level in the skewness spectrogram can be exactly determined. This affects the symmetric distribution from the left side of the distribution in Step 2, and the errors of the retrieved brightness temperature can be minimized. Therefore, the proposed method is an excellent candidate for RFI elimination compared with the conventional method, which uses the threshold level with the mean value and standard deviation. The proposed method will be applied to sea salinity measurements along a coastline, and the performances in different RFI environments will be reported in the future.

Author Contributions: Conceptualization, Y.-H.K. and M.O.; methodology, M.O.; software, M.O.; validation, M.O.; formal analysis, M.O. and Y.-H.K.; investigation, M.O.; resources, M.O. and Y.-H.K.; data curation, M.O.; writing—original draft preparation, M.O.; writing—review and editing, M.O. and Y.-H.K.; visualization, M.O.; supervision, Y.-H.K.; project administration, Y.-H.K.; funding acquisition, Y.-H.K.

References

1. Oliva, R.; Daganzo-Eusebio, E.; Kerr, Y.; Mecklenburg, S.; Nieto, S.; Richaume, P.; Gruhier, C. SMOS radio frequency interference scenario: status and actions taken to improve the RFI environment in the 1400-1427-MHz passive band. *IEEE Trans. Geosci. Remote Sens.* **2012**, 50, 1427–1439.
2. Ruf, C.; Gross, S.; Misra, S. RFI detection and mitigation for microwave radiometry with an agile digital detector. *IEEE Trans. Geosci. Remote Sens.* **2006**, 44, 694–706.
3. Roo, R.; Misra, S.; Ruf, C. Sensitivity of the kurtosis statistic as a detector of pulsed sinusoidal RFI. *IEEE Trans. Geosci. Remote Sens.* **2007**, 45, 1938–1946.
4. Roo, R.; Misra, S. A demonstration of the effects of digitization on the calculation of kurtosis for the detection of RFI in microwave radiometry. *IEEE Trans. Geosci. Remote Sens.* **2008**, 46, 3129–3136.
5. Guner, B.; Frankford, M.; Johnson, J. A study of the Shapiro-Wilk test for the detection of pulsed sinusoidal radio frequency interference. *IEEE Trans. Geosci. Remote Sens.* **2009**, 47, 1745–1751.
6. Tarongi, J.; Camps, A. Normality analysis for RFI detection in microwave radiometry. *Remote Sens.* **2009**, 2, 191–210.
7. Ellingson, S.; Hampson, G.; Johnson, J. Design of an L-band microwave radiometer with active mitigation of interference. *International Geoscience and Remote Sensing Symposium.* **2013**, 3, 1751–1753.
8. Niamsuwan, N.; Johnson, J.; Ellingson, S. Examination of a simple pulse blanking technique for RFI mitigation. *Radio Science*, **2005**, 40, 1–11.
9. Guner, B.; Johnson, J.; Niamsuwan, N. Time and frequency blanking for radio-frequency interference mitigation in microwave radiometry. *IEEE Trans. Geosci. Remote Sens.* **2007**, 45, 3672–3679.
10. Aksoy, M.; Johnson, J.; Misra, S.; Colliander, A.; O'Dwyer, I. L-Band radio-frequency interference observations during the SMAP validation experiment 2012. *IEEE Trans. Geosci. Remote Sens.* **2016**, 54, 1323–1335.

11. Fanise, P.; Pardé, M.; Zribi, M.; Dechambre, M.; Caudoux, C. Analysis of RFI identification and mitigation in CAROLS radiometer data using a hardware spectrum analyser. *Sensors*, **2011**, 11, 3037–3050.

12. Piepmeier, J.; Johnson, J.; Mohammed, P.; Bradley, D.; Ruf, C.; Aksoy, M.; Garcia, R.; Hudson, D; Miles, L.; Wong, M. Radio-frequency interference mitigation for the soil moisture active passive microwave radiometer. *IEEE Trans. Geosci. Remote Sens.* **2014**, 52, 761–775.

13. Tarongi, J.; Camps, A. Radio frequency interference detection and mitigation algorithms based on spectrogram analysis. *Algorithms*. **2011**, 4, 239–261.

14. Ulaby F.; Moore, R.; Fung, A. *Microwave Remote Sensing: Active and Passive, Volume I: Fundamentals and Radiometry*. Norwood, Mass: Artech House Publishers. **1986**, 358–376.

15. Frater, R.; Williams D. An active 'cold' noise source. *IEEE Trans. Microw. Theory Techn.* **1981**, 29, 344–347.

16. Schwank, M.; Wiesmann, A; Werner, C; Matzler, C; Weber, D; Murk, A.; Volksch, I; Wegmuller, U. ELBARA II, an L-band radiometer system for soil moisture research. *Sensors*, **2009**, 10, 584–612.

17. Goodberlet, M.; Mead, J. Two-load radiometer precision and accuracy. *IEEE Trans. Geosci. Remote Sens.* **2006**, 44, 58–67.